# Activity of CeOx and TiOx Nanoparticles Grown on Au(111) in the Water-Gas Shift Reaction

J. A. Rodriguez, *et al.*

*Science* **318**, 1757 (2007);
DOI: 10.1126/science.1150038



*Science* (print ISSN 0036-8075; online ISSN 1095-9203) is published weekly, except the last week in December, by the American Association for the Advancement of Science, 1200 New York Avenue NW, Washington, DC 20005. 

9. P. G. Jasien, C. E. Dykstra, *J. Am. Chem. Soc.* **105**, 2089 (1983).
10. L. A. Tjurina *et al.*, *Organometallics* **23**, 1349 (2004).
11. C. Jones, P. C. Junk, J. A. Platts, A. Stasch, *J. Am. Chem. Soc.* **128**, 2206 (2006).
12. S. P. Green, C. Jones, P. C. Junk, K.-A. Lippert, A. Stasch, *Chem. Commun.* 3978 (2006).
13. L. Bourget-Merle, M. F. Lappert, J. R. Severn, *Chem. Rev.* **102**, 3031 (2002).
14. Materials and methods are available on *Science* Online.
15. J. Prust *et al.*, *Z. Anorg. Allg. Chem.* **627**, 2032 (2001).
16. Crystal data for **1** and **2** were obtained at 123(2) K with use of an Enraf-Nonius Kappa charge-coupled device diffractometer and $MoK_\alpha$ radiation ($\lambda = 0.71073$ Å). The crystal data are as follows. For **1**: $a = b = 18.409(3)$ Å, $c = 17.640(4)$ Å, tetragonal, $I4_1/a$, $Z = 4$, $R_1$ for 3176 [data intensity $I > 2\sigma(I)$] unique data = 0.0448, and $wR_2$ (all 4353 unique data) = 0.1256. For **2**: $a = 14.444(3)$ Å, $b = 14.203(3)$ Å, $c = 26.742(5)$ Å, $\beta = 94.87(3)°$, monoclinic, $P2_1/c$, $Z = 4$, $R_1$ for 9054 [data intensity $I > 2\sigma(I)$] unique data = 0.0428, and $wR_2$ (all 11,843 unique data) = 0.1145.
17. As determined from a survey of the Cambridge Crystallographic Database, September 2007.
18. K. P. Huber, G. Herzberg, *Constants of Diatomic Molecules* (Van Nostrand, New York, 1979), pp. 116 and 394.
19. J. Emsley, *The Elements* (Clarendon, Oxford, ed. 2, 1995).
20. M. A. G. M. Tinga *et al.*, *J. Am. Chem. Soc.* **115**, 2808 (1993).
21. Y. Wang *et al.*, *J. Am. Chem. Soc.* **127**, 11944 (2005).
22. J. Chai *et al.*, *J. Am. Chem. Soc.* **127**, 9201 (2005).
23. R. E. Mulvey *et al.*, *Chem. Commun.* 376 (2002).
24. E. C. Ashby, A. B. Goel, *Inorg. Chem.* **18**, 1306 (1979).
25. M. J. Frisch *et al.*, Gaussian 98, Revision A.10, Gaussian, Incorporated, Pittsburgh, PA (2001).
26. Z. Zhu *et al.*, *Angew. Chem. Int. Ed.* **45**, 5807 (2006).
27. M.-H. Baik, R. A. Friesner, G. Parkin, *Polyhedron* **23**, 2879 (2004).
28. A recent precedent for these reactions exists with the insertions of the carbodiimide, CyN=C=NCy, into the Fe-B bonds of terminal iron borylene complexes, e.g., $(C_5H_5)Fe(CO)_2(BNCy_2)$, to give ferro-amidinate complexes of boron, e.g., $[(C_5H_5)Fe(CO)_2C(NCy)_2]BNCy_2$. These reactions are thought to proceed via initial N-coordination of the carbodiimide at the borylene center (*29*).
29. G. A. Pierce *et al.*, *Angew. Chem. Int. Ed.* **46**, 2043 (2007).


30. We are grateful to the Australian Research Council for providing fellowships to C.J. and A.S. We also thank the Engineering and Physical Sciences Research Council of the UK for a partly funded studentship (S.P.G.). Metrical data for $(Priso)Mg(\mu\text{-}I)_2Mg(OEt_2)(Priso)\cdot(hexane)_{0.5}$, **1**, **2**, and **5**·$(toluene)_2$ are freely available from the Cambridge Crystallographic Database Center (CCDC codes 661565 to 661568).


**Supporting Online Material**

www.sciencemag.org/cgi/content/full/1150856/DC1
Materials and Methods
Figs. S1 to S4
Tables S1 to S3
References


24 September 2007; accepted 26 October 2007
Published online 8 November 2007;
10.1126/science.1150856
Include this information when citing this paper.


# Activity of $CeO_x$ and $TiO_x$ Nanoparticles Grown on Au(111) in the Water-Gas Shift Reaction


**J. A. Rodriguez,[1]* S. Ma,[1] P. Liu,[2] J. Hrbek,[1] J. Evans,[3] M. Pérez[3]**



**The high performance of Au-$CeO_2$ and Au-$TiO_2$ catalysts in the water-gas shift (WGS) reaction ($H_2O + CO \rightarrow H_2 + CO_2$) relies heavily on the direct participation of the oxide in the catalytic process. Although clean Au(111) is not catalytically active for the WGS, gold surfaces that are 20 to 30% covered by ceria or titania nanoparticles have activities comparable to those of good WGS catalysts such as Cu(111) or Cu(100). In $TiO_{2-x}$/Au(111) and $CeO_{2-x}$/Au(111), water dissociates on O vacancies of the oxide nanoparticles, CO adsorbs on Au sites located nearby, and subsequent reaction steps take place at the metal-oxide interface. In these inverse catalysts, the moderate chemical activity of bulk gold is coupled to that of a more reactive oxide.**


Nearly 95% of the hydrogen supply is produced from the reforming of crude oil, coal, natural gas, wood, organic wastes, and biomass (*1*), but this reformed fuel contains 1 to 10% CO, the presence of which degrades the performance of the Pt electrode in fuel cell systems (*2*). To get clean hydrogen for fuel cells and other industrial applications, the water-gas shift (WGS) reaction ($CO + H_2O \rightarrow CO_2 + H_2$) is critical. Current industrial catalysts for the WGS (mixtures of Fe-Cr or Zn-Al-Cu oxides) are pyrophoric and normally require lengthy and complex activation steps before usage (*3*). Au-$CeO_2$ and Au-$TiO_2$ nanomaterials have recently been reported to be very efficient catalysts for the WGS (*3*–*5*). This is remarkable because neither bulk Au (*6*) nor bulk ceria and titania are known as WGS catalysts (*3*, *4*).

The nature of the active phase(s) in these metal/oxide nanocatalysts and the WGS reaction mechanism are still unclear. For example, the as-prepared Au-$CeO_2$ catalysts contain nanoparticles of pure gold and gold oxides ($AuO_x$) dispersed on a nanoceria support. Each of these gold species could be in the active phase (*3*–*5*), and the ceria support may not be a simple spectator in these systems (*7*). Although pure ceria is a very poor WGS catalyst, the properties of this oxide were found to be crucial for the observed activity of the Au-$CeO_2$ nanocatalysts (*4*, *6*, *8*). Several studies dealing with metal/oxide powder catalysts and the WGS reaction indicate that the oxide plays a direct role in the reaction (*3*, *4*, *9*, *10*), but because of the complex nature of these systems, there is no agreement on its role. Thus, we performed a series of experiments to test the chemical and catalytic properties of $CeO_2$ and $TiO_2$ nanoparticles (NPs) dispersed on a Au(111) template, as inverse model catalysts. Results of density-functional calculations point to a very high barrier for the dissociation of $H_2O$ on Au(111) or Au(100) (*11*), which leads to negligible activity for the WGS process. Even gold NPs cannot dissociate water and catalyze the WGS reaction (*11*).

Part of the experiments described below were carried out in ultrahigh-vacuum (UHV) chambers that have attached a batch reactor (*12*) or have capabilities for scanning tunneling microscopy (STM) (*13*). High-resolution x-ray photoelectron spectroscopy (XPS) spectra, probing only the near-surface region in the oxide/gold systems (*5*, *14*), were acquired at the U7A beamline of the National Synchrotron Light Source. To prepare the $TiO_2$/Au(111) surfaces, Ti atoms were vapor deposited on a gold substrate covered with $NO_2$ at 100 K (*15*). The temperature was then raised to 700 K and the $TiNO_x$ particles were transformed into $TiO_2$. STM images indicated that this methodology produces flat NPs of $TiO_2$ exhibiting a combination of rutile and anatase phases (*15*). The NPs of ceria were prepared according to two different procedures. In the first one, labeled $CeO_2$-I here, alloys of $CeAu_x$/Au(111) were exposed to $O_2$ ($\sim 5 \times 10^{-7}$ torr) at 500 to 700 K for 5 to 10 min (*13*, *14*). The $CeO_2$ NPs grew dispersed on the herringbone structure of Au(111) (Fig. 1A) and had a rough three-dimensional structure that did not exhibit any particular face of ceria (Fig. 1B). In the second procedure, labeled $CeO_2$-II here, Ce was vapor deposited onto Au(111) under an atmosphere of $O_2$ ($\sim 5 \times 10^{-7}$ torr) at 550 K and then heated to 700 K. In these cases, the $CeO_2$ NPs grew preferentially at the steps between the terraces in the Au(111) substrate (Fig. 1C) and displayed regions with a $CeO_2$(111) orientation. When there was a deficiency of oxygen, groups or clusters of O vacancies were seen in STM images (Fig. 1D). This result is similar to that found for bulk $CeO_{2-x}$(111) (*16*). High-resolution XPS showed that Au atoms do not incorporate into the ceria lattice (*14*). Gold 4f spectra taken at photon energies of 240 to 380 eV, probing only two to three layers near the surface, showed the absence of the features expected for Au cations incorporated into ceria (*5*).

In Fig. 2, the WGS activity of a series of $TiO_2$/Au(111), $CeO_2$-I/Au(111), and $CeO_2$-II/Au(111) surfaces is shown. The fraction of the Au(111) substrate covered by the $TiO_2$ or $CeO_2$ particles was determined by means of ion-scattering spectroscopy (*5*, *7*). In the kinetics measurements, the sample was transferred from the


[1]Chemistry Department, Brookhaven National Laboratory, Upton, NY 11973, USA. [2]Center for Functional Nanomaterials, Brookhaven National Laboratory, Upton, NY 11973, USA. [3]Facultad de Ciencias, Universidad Central de Venezuela, Caracas, 1020-A Venezuela.

*To whom correspondence should be addressed. E-mail: rodrigez@bnl.gov

UHV chamber to the batch reactor at ~300 K, then the reactant gases were introduced (20 torr of CO and 10 torr of $H_2O$) and the sample was rapidly heated to the reaction temperature (575 K). Product yields were analyzed by a gas chromatograph (*17*). The amount of product was normalized by the active area exposed by the front of the sample. The sample holder was passivated by extensive sulfur poisoning (exposure to $H_2S$) and had no catalytic activity (*6*). XPS spectra showed that there was no migration of S from the sample holder to the oxide/gold surfaces. The values reported in Fig. 2 were acquired after 5 min of reaction. In our batch reactor, a steady-state regime for the production of $H_2$ and $CO_2$ was reached after 1 to 2 min of reaction time. The kinetics experiments were done in the limit of low conversion (<5%).

The data in Fig. 2 show a substantial increase in catalytic activity at small coverages of $CeO_2$ and $TiO_2$. Although clean Au(111) is not catalytically active, gold surfaces that are 20 to 30% covered by the oxide NPs had activities per unit geometric area similar to or larger than those of Cu(111) or Cu(100) under similar conditions (*6*, *17*), noting that Cu is the best known metal catalyst for the WGS (*11*, *17*, *18*).

In Fig. 2, the catalytic activity of the surface reaches a maximum, then decreases and disappears once there is no Au exposed and multilayers of ceria or titania cover the metal substrate (*13*–*15*). As we discuss below, small oxide NPs exhibit the highest chemical reactivity toward CO and $H_2O$. In general, the effects of ceria on the catalytic activity are greater than those of titania, with $TiO_2$/Au(111) being as active as Cu(100). In Fig. 2, we compare the relative WGS activities of the $CeO_2$-I/Au(111) and $CeO_2$-II/Au(111) surfaces. The procedure followed to prepare the $CeO_2$-I/Au(111) surfaces yielded a greater dispersion for the oxide NPs on the gold template (compare Fig. 1, A and C), and the NPs had a more disordered structure (compare Fig. 1, B and D). These morphological differences could account for a superior catalytic activity for the $CeO_2$-I/Au(111) systems.

After collecting the kinetics data, the gases were pumped out from the reaction cell and the surfaces were characterized with XPS, which showed adsorbed $CO_x$ groups with a C 1s binding energy of 289.6 to 289.9 eV. This binding energy matches well those found for formate (HCOO) and carbonate ($CO_3$) groups bonded to oxides (*19*, *20*). The XPS data also indicated a lack of oxidation of the Au substrate. The catalysts exhibited Au 4f spectra that were practically identical to those of Au(111) and very different from those expected for $AuO_x$ species or Au incorporated into the ceria lattice (*4*, *5*). The lack of oxidation of the Au substrate seen in the XPS data are consistent with in situ measurements of near-edge x-ray absorption spectroscopy for high–surface area catalysts (*3*, *5*), which show that $Au^{\delta+}$ species are not stable under typical WGS conditions.

For the surfaces that have the highest activity in Fig. 2 (the fraction of Au covered < 30%), the Ce 3d and Ti 2p core-level XPS spectra showed a significant reduction of the oxides upon exposure of $CeO_2$/Au(111) and $TiO_2$/Au(111) to the reactants of the WGS. After curve-fitting (*7*, *14*) the corresponding Ce 3d and Ti 2p spectra, we found that 14 to 17% of the O atoms in the $CeO_2$ and $TiO_2$ NPs were removed to produce partially reduced ceria and titania. The degree of reduction of the $CeO_2$ and $TiO_2$ NPs substantially decreased when the fraction of gold covered by the oxide increased above 35%. As an example, we show in Fig. 3 the percentage of O vacancies in ceria after performing the WGS on the $CeO_2$-I/Au(111) catalysts: The systems with a high catalytic activity also have a significant concentration of O vacancies and associated $Ce^{3+}$ cations.

The high catalytic activity for low coverages of ceria and titania can be attributed to special chemical properties of the oxide NPs and cooperative effects at oxide-metal interfaces. However, it is very difficult to quantify the number of active sites in the oxide/gold catalysts of Figs. 1 and 2. The reaction likely involves O vacancies that are near oxide-gold interfaces. Because O vacancies tend to form groups or ensembles (Fig. 1D) (*16*, *21*), uncovering in this way the metal substrate, oxide-gold interfaces can exist within the oxide NPs. We estimate that the best catalysts in Fig. 2 have a turnover frequency (TOF) that is 40 to 50 times as large as that of Cu(100) (*22*).

Using density-functional theory (DFT) (*11*, *23*, *24*), we investigated the WGS reaction on Au(100) or Au(111), a free $Ti_2O_4$ cluster [see structure in (*25*)], a free $TiO_2$ single chain, and over a model $TiO_2$/Au(111) catalyst that contains chains of $TiO_2$ over the gold substrate in a (3 × 1) array (Fig. 4). This model catalyst exposes not fully coordinated Ti centers, as expected for a $TiO_2$ NP, and allows the study of the oxide-metal interface. A very high barrier for the dissociation of water on Au(111) or Au(100) was seen (Fig. 4), but once OH formed, subsequent steps for the WGS process occurred readily on the gold substrate.

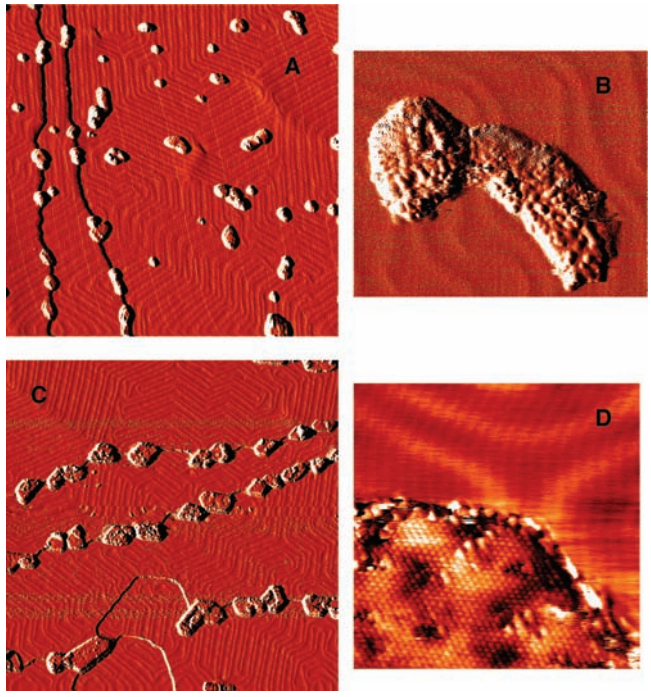


**Fig. 1.** (**A**) STM image taken after oxidizing a Ce-Au(111) alloy in $O_2$ at 550 K and subsequent annealing to 690 K. Size: 200 nm by 200 nm; imaging parameters: −1.970 V and 0.03182 nA. (**B**) STM image also taken after oxidizing a Ce-Au(111) alloy in $O_2$. Size: 30 nm × 25 nm; imaging parameters: −1.709 V and 0.02761 nA. (**C**) STM image acquired after depositing Ce in an atmosphere of $1.5 \times 10^{-7}$ torr of $O_2$ at 550 K followed by annealing to 700 K. Size: 200 nm by 200 nm; imaging parameters: 2.463 V and 0.02597 nA. (**D**) STM image also recorded after depositing Ce in an atmosphere of $1.5 \times 10^{-7}$ torr of $O_2$ at 550 K followed by annealing to 700 K. Size: 15 nm by 15 nm; imaging parameters: 0.806 V and 0.04404 nA

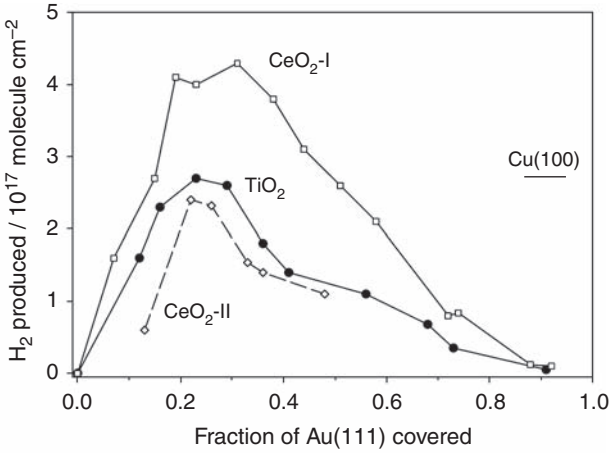


**Fig. 2.** Production of hydrogen during the WGS reaction on a Au(111) surface partially covered with ceria or titania. The ceria NPs were prepared according to two different methodologies denoted as $CeO_2$-I and $CeO_2$-II (see text). Each surface was exposed to a mixture of 20 torr of CO and 10 torr of $H_2O$ at 573 K for 5 min.

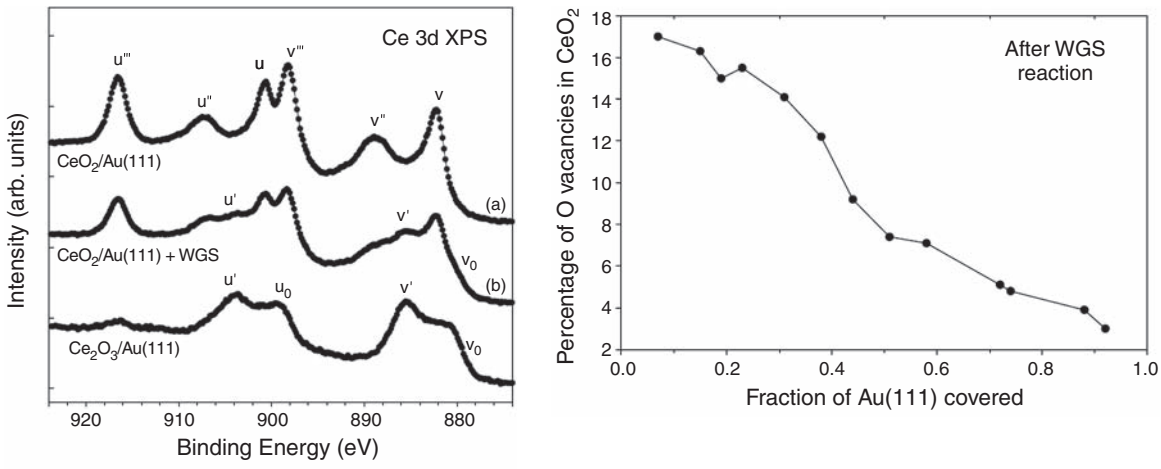


**Fig. 3.** (**Left**) Ce 3d XPS spectra taken before (trace a) and after (trace b) exposing a $CeO_2$-I/Au(111) surface to the WGS reaction. The fraction of the Au surface covered by ceria was ~30%. For comparison, we show the corresponding spectrum for a $Ce_2O_3$/Au(111) system. (**Right**) Percentage of O vacancies in the $CeO_2$-I/Au(111) catalysts after the WGS reaction (20 torr of CO, 10 torr of $H_2O$ at 573 K for 5 min). The amount of oxygen removed from the ceria was calculated by curve-fitting (*5*, *7*, *14*) the corresponding Ce 3d spectra and obtaining the ratio of $Ce^{3+}/Ce^{4+}$ cations.

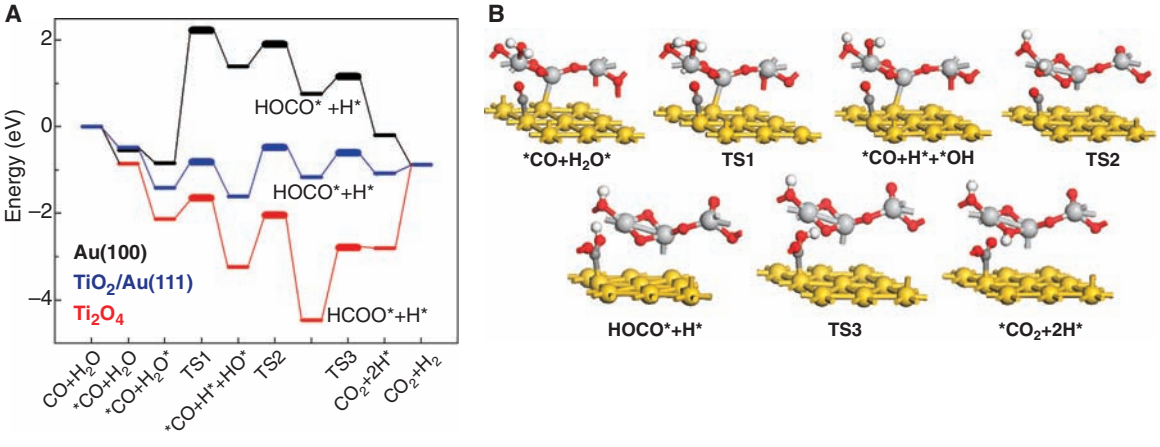


**Fig. 4.** (**A**) Calculated reaction profile for the WGS on Au(100), a free $Ti_2O_4$ cluster, and $TiO_2$/Au(111) model catalysts. Transitions states are denoted as TS1, TS2, and TS3. (**B**) Optimized structures for the different steps of the WGS on $TiO_2$/Au(111). Large yellow spheres, Au; large gray spheres, Ti; small red spheres, O; small white spheres, H; small dark gray spheres, C. Adsorbed species are denoted by asterisks (*).

Indeed, experimental studies show that CO adsorbs and is chemically active on gold surfaces first covered with oxygen or other chemical species (*26*, *27*). On a free $Ti_2O_4$ cluster or on a nonsupported $TiO_2$ single chain, the dissociation of water is not difficult, and is even easier than on Cu(100) (Fig. 4), but the reaction of the formed OH with CO leads to the formation of a stable formate species that prevents the production of $H_2$ and $CO_2$.

The DFT calculations for the model $TiO_2$/Au(111) catalyst show a system that can readily perform the WGS process (Fig. 4). The reaction pathway with the minimum-energy barriers involves the following steps:

$$CO_{gas} \rightarrow CO_{ads} \quad (1)$$

$$H_2O_{gas} \rightarrow H_2O_{ads} \quad (2)$$

$$H_2O_{ads} \rightarrow OH_{ads} + H_{ads} \quad (3)$$

$$CO_{ads} + OH_{ads} \rightarrow HOCO_{ads} \quad (4)$$

$$HOCO_{ads} \rightarrow CO_{2,gas} + H_{ads} \quad (5)$$

$$2H_{ads} \rightarrow H_{2,gas} \quad (6)$$

The adsorption and dissociation of water take place on the oxide, whereas CO adsorbs on sites of the gold substrate located nearby (bifunctional catalyst). All of the subsequent steps occur at an oxide-metal interface. The DF calculations show that the activation energy for the dissociation of water on $TiO_2$/Au(111), ~0.6 eV, is also much smaller than on Cu(100), ~1.1 eV (*11*), so $TiO_2$/Au(111) should be a better WGS catalyst than Au(100) and Cu(100), as found above. The intermediate that precedes the formation of $CO_2$ and $H_2$ in the WGS process is a HOCO species. $CO_x$ species were observed experimentally on the surface of the catalysts after the WGS, and they could be simple spectators when strongly bound to the oxide nanoparticles.

Our results imply that the high performance of Au-$CeO_2$ and Au-$TiO_2$ catalysts in the WGS (*4*, *6*) relies heavily on the direct participation of the oxide-metal interface in the catalytic process. The oxide helps in the dissociation of water, a reaction that extended surfaces and NPs of gold cannot perform (*11*). Experiments in our laboratories have verified that $TiO_{2-x}$/Au(111) and $CeO_{2-x}$/Au(111) easily dissociate water, and no decomposition of this adsorbate is seen when no O vacancies exist in the oxide nanoparticles (*14*). Exposure of small coverages of $TiO_2$ and $CeO_2$ to CO at 575 K leads to the appearance of O vacancies in the oxide NPs, and these systems become active for the dissociation of water. For the WGS, it is critical that the properties of the oxide facilitate $H_2O$ dissociation, and we have found that this is the case for NPs of $CeO_{2-x}$, $TiO_{2-x}$, $MoO_{3-x}$, and $ZnO_{1-x}$.

Previous studies indicate that overlayers of Au can be catalytically active for the oxidation of CO, if they are nanosized in one dimension or interact strongly with an oxide support (*28*). In contrast, the situation for the WGS on $TiO_{2-x}$/Au(111) and $CeO_{2-x}$/Au(111) takes advantage of the moderate chemical activity of bulk gold by coupling it to that of a more reactive oxide material.

### References and Notes


1. J. J. Spivey, *Catal. Today* **100**, 171 (2005).
2. D. J. Suh, C. Kwak, J. H. Kim, S. Kwon, T. J. Park, *J. Power Sources* **142**, 70 (2005).
3. R. Burch, *Phys. Chem. Chem. Phys.* **8**, 5483 (2006).
4. Q. Fu, H. Saltsburg, M. Flytzani-Stephanopoulos, *Science* **301**, 935 (2003).
5. X. Wang, J.A. Rodriguez, J.C. Hanson, M. Perez, J. Evans, *J. Chem. Phys.* **123**, 221 101 (2005).
6. J. A. Rodriguez, P. Liu, J. Hrbek, J. Evans, M. Perez, *Angew. Chem. Int. Ed.* **46**, 1329 (2007).
7. J. A. Rodriguez, M. Pérez, J. Evans, G. Liu, J. Hrbek, *J. Chem. Phys.* **122**, 241101 (2005).
8. Q. Fu, W. Deng, H. Saltsburg, M. Flytzani-Stephanopoulos, *Appl. Catal. B: Environ.* **56**, 57 (2005).
9. S. Ricote *et al.*, *Appl. Catal. Gen.* **303**, 35 (2006).
10. T. Bunluesin, R. J. Gorte, G. W. Graham, *Appl. Catal. Environ.* **15**, 107 (1998).
11. P. Liu, J. A. Rodriguez, *J. Chem. Phys.* **126**, 164705 (2007).

12. The sample could be transferred between the reactor and UHV chamber without exposure to air (*5*, *6*). The UHV chamber (base pressure ~ $1 \times 10^{-10}$ torr) was equipped with instrumentation for XPS, low-energy electron diffraction, ion-scattering spectroscopy, and thermal-desorption mass spectroscopy.
13. S. Ma, X. Zhao, J. A. Rodriguez, J. Hrbek, *J. Phys. Chem. C* **111**, 3685 (2007).
14. X. Zhao, S. Ma, J. Hrbek, J. A. Rodriguez, *Surf. Sci.* **601**, 2445 (2007).
15. Z. Song, J. Hrbek, R. Osgood, *Nano Lett.* **5**, 1327 (2005).
16. F. Esch *et al.*, *Science* **309**, 752 (2005).
17. J. Nakamura, J. M. Campbell, C. T. Campbell, *J. Chem. Soc. Faraday Trans.* **86**, 2725 (1990).
18. C. V. Ovesen, P. Stoltze, J. K. Nørskov, C. T. Campbell, *J. Catal.* **134**, 445 (1992).
19. J. Zhou, D. R. Mullins, *Surf. Sci.* **600**, 1540 (2006).
20. C. T. Au, W. Hirsch, W. Hirschwald, *Surf. Sci.* **197**, 391 (1988).
21. O. Dulub *et al.*, *Science* **317**, 1052 (2007).
22. To estimate the TOF of $CeO_{2-x}$/Au(111) surfaces, we took into account the area covered by the oxide NPs and the concentration of O vacancies. It was assumed that all the atoms of a flat Cu(100) surface are active in the WGS reaction. This is a common assumption (*17*, *18*).
23. The unrestricted DF calculations were performed with the DMol3 code, treating molecules, nanostructures, and extended surfaces with the same level of accuracy (*11*, *24*). Au(100), Au(111), and $TiO_2$/Au(111) were modeled by means of the supercell approach with three-layer gold slabs and an 11 Å vacuum between the slabs (*11*). The top layer of the Au substrate, the oxide nanostructures, and the adsorbates were allowed to fully relax.
24. B. Delley, *J. Chem. Phys.* **92,** 508 (1990); **113,** 7756 (1992).
25. T. Albaret, F. Finocchi, C. Noguera, *Faraday Discuss.* **114**, 285 (1999).
26. V. A. Bondzie, S. C. Parker, C. T. Campbell, *Catal. Lett.* **63**, 143 (1999).
27. B. K. Min, C. M. Friend, *Chem. Rev.* **107**, 2709 (2007).
28. M. S. Chen, D. W. Goodman, *Science* **306**, 252 (2004).
29. N. C. Hernández, J. F. Sanz, J. A. Rodriguez, *J. Am. Chem. Soc.* **128**, 15600 (2006).
29. The work performed at Brookhaven National Laboratory was supported by the U.S. Department of Energy, Office of Basic Energy Sciences, under contract DE-AC02-98CH10886. J.E. and M.P. are grateful to Intevep for partial support of the work carried out at the Universidad Central de Venezuela.

4 September 2007; accepted 22 October 2007
10.1126/science.1150038

# Accretion of Mudstone Beds from Migrating Floccule Ripples

**Juergen Schieber,[1]* John Southard,[2] Kevin Thaisen[1]**

**Mudstones make up the majority of the geological record. However, it is difficult to reconstruct the complex processes of mud deposition in the laboratory, such as the clumping of particles into floccules. Using flume experiments, we have investigated the bedload transport and deposition of clay floccules and find that this occurs at flow velocities that transport and deposit sand. Deposition-prone floccules form over a wide range of experimental conditions, which suggests an underlying universal process. Floccule ripples develop into low-angle foresets and mud beds that appear laminated after postdepositional compaction, but the layers retain signs of floccule ripple bedding that would be detectable in the rock record. Because mudstones were long thought to record low-energy conditions of offshore and deeper water environments, our results call for reevaluation of published interpretations of ancient mudstone successions and derived paleoceanographic conditions.**

A century ago, Henry Clifton Sorby, one of the pioneers of geology, pointed to the study of muds as one of the most challenging topics in sedimentary geology (*1*). Today, with our knowledge clearly expanded, muddy sediments are still considered highly complex systems that may require as many as 32 variables and parameters for a satisfactory physicochemical characterization (*2*). More research may clarify interdependencies between a number of these parameters and may allow us to consider a smaller number of variables, but the fundamental complexity of muddy sediments is likely to remain. A key issue in mudstone sedimentation is flocculation, a phenomenon in which a number of these parameters, such as settling velocity, floccule size, grain-size distribution, ion exchange behavior, and organic content "come together." A joining of smaller particles to form larger aggregates, flocculation enhances the deposition rate of fine-grained sediments, and its understanding is critical for modeling the behavior of mud in sedimentary environments.

Flocculation is affected by particle concentration within the fluid and intensity of turbulence (*3*, *4*). Over time, floccules enlarge to a maximum equilibrium diameter that is related to the intensity of turbulence (*5*). Floccule deposition is influenced by turbulence, bed shear stress, sediment concentration, and settling velocity. We currently still miss critical data on floccule formation and on the influence of floccule structure and turbulence on the formation of muddy sediments (*6*). We will collect data concerning these issues with new instrumentation in the near future, although the importance of our observations will not be affected. The notion is widely held that slow-moving currents or still water are a prerequisite for substantial mud deposition (*7*, *8*) because shear stress in swift-moving currents disrupts previously formed fragile floccules and prevents their deposition, but our observations suggest an alternative mode of mud deposition that apparently left its imprint in the rock record.

Mudstones constitute up to two-thirds of the sedimentary record and are arguably the most poorly understood type of sedimentary rocks (*9*). Mudstone successions contain a wealth of sedimentary features that provide information about depositional conditions and sedimentary history (*10*–*13*), but presently we lack the information that would allow us to link features observed in the rock record to measurable sets of physical variables in modern environments.

Although various small-scale sedimentary structures have been described from modern muds, these have not been observed in the making. This forces us to infer controlling parameters (e.g., current velocity and density of suspension) from temporally and spatially very limited measurements in the overlying water column (*14*–*17*). Such measurements (e.g., flow velocity, sediment concentration) in modern environments are commonly considered representative of depositional conditions for the uppermost millimeters to decimeters of the accumulating deposits. However, upon close examination, modern sediments show considerable heterogeneity at the millimeter to centimeter scale (*16*), an indication that what we observe in surficial sediments is not a direct response to measured conditions in the overlying water column. To improve on this situation, it is essential to conduct experiments that replicate natural conditions and to compare the experimental sediments to the rock record.

Here, we report experimental insights into the sedimentology of mudstones. In past experimental studies, centrifugal pumps were used to recirculate mud suspensions (*18*–*20*), destroying the clay floccules that are of such key importance in mud transport and deposition. Therefore, to minimize the risk of shredding clay floccules once formed, we built a racetrack flume that uses a paddle belt (*21*) for moving the mud suspension.

The racetrack flume (fig. S1) used for these experiments (*21*) has a 25-cm-wide channel. The effective flow depth was 5 cm. Powdered kaolinite clay (Fig. 1A) was mixed with water and added into the flume, running at 50 cm/s velocity (*21*). Sediment concentrations ranging from 0.03 g/l to 2 g/l were explored, and suspended sediment concentrations were monitored with an optical turbidity sensor. Experiments were conducted in distilled water, fresh (tap) water, and salt water (35 per mil salinity). In a few experiments, Ca-montmorillonite and natural lake mud (sieved to 63 μm) was used.

Addition of clay to the flume resulted within minutes in the formation of "floccule streamers" that mark boundary-layer streaks (*22*). Floccules range in size from 0.1 mm to almost 1 mm (Fig. 1, B to D) and were sampled and examined with a scanning electron microscope (SEM). After establishment of a stable suspended clay concentration, the velocity was stepwise reduced (Fig. 2) until the critical velocity of sedimentation was reached (*23*). At that point, a linear decline of sediment concen-

[1]Department of Geological Sciences, Indiana University, Bloomington, IN 47405, USA. [2]Department of Earth and Planetary Sciences, Massachusetts Institute of Technology, Cambridge, MA 02139, USA.

*To whom correspondence should be addressed. E-mail: jschiebe@indiana.edu